

Enhancing Electrochemical CO₂ Reduction using Ce(Mn,Fe)O₂ with La(Sr)Cr(Mn)O₃ Cathode for High-Temperature Solid Oxide Electrolysis Cells

Seokhee Lee, Minkyu Kim, Kang Taek Lee,* John T. S. Irvine, and Tae Ho Shin*

Robust oxide electrodes with high activity and durability have attracted significant attention as alternatives for Ni-based cathodes in high-temperature solid oxide electrolysis cells (SOECs). Noncoking La(Sr)Cr(Mn)O₃ (LSCM)-based oxide cathodes have shown promise as durable ceramic cathodes; however, they suffer from low electrocatalytic activities in electrochemical CO₂ reduction. In this study, a dual-phase composite electrode consisting of LSCM and Ce(Mn, Fe)O₂ (CMF) is developed to enhance the electrocatalytic activity of CO₂ reduction in SOECs. The developed electrode shows excellent electrolysis performance of 2.64 and 1.22 A cm⁻² at 1123 K, when voltages of 1.5 and 1.2 V are applied, respectively, without using any precious metal catalysts. The enhanced electrolysis performance is attributed to increases in electrocatalytic activity and surface oxygen vacancies caused by the CMF, which accelerates CO₂ adsorption and results in the subsequent dissociation of the carbonate intermediate in the CO₂ reduction.

environmental impact of the reduced CO₂ emissions and formulate better energy strategies for the post-COVID-19 world.^[1,2] CO₂ capture and storage technology has been extensively investigated for reducing carbon emissions. The more recent CO₂ capture, utilization, and storage (CCUS) approach also considers the utilization of excess CO₂ recovered from industrial emissions. In the simplest case, CO₂ can be converted into CO, which is an important bulk chemical for several applications. Moreover, through the electrochemical reduction of CO₂ to CO, the excess electrical energy generated from renewable sources, which tend to be intermittent in nature, can be stored in the form of hydrocarbons and other chemicals for use as feedstock in energy production.

1. Introduction

Reducing CO₂ emissions has become crucial for mitigating climate changes related to global warming, in order to overcome the unprecedented crises in terms of sustainability. The current global lockdown to combat the coronavirus disease (COVID-19) pandemic has resulted in a drastic reduction in CO₂ emissions, which provides an opportunity to further study the

This advanced CCUS method consumes CO₂ and promotes the development of renewable energy.^[3–7] Aqueous electrolysis and its modified versions incorporating photocatalysis have been widely explored as promising routes to realize the electrochemical reduction of CO₂ at ambient temperature.^[8] However, there remain several critical drawbacks such as the need for precious metals in the catalysts, catalyst deactivation by the carbon-based support, and slow reaction kinetics due to the low solubility of CO₂ in aqueous electrolytes.^[7,9–11] In comparison, high-temperature CO₂ electrolysis using solid oxide electrolysis cells (SOECs) has attracted significant attention owing to its high efficiency.^[3–7,12,13] The solid electrolyte in SOECs has oxygen vacancies and can conduct oxide ions at high and intermediate temperatures (773–1273 K), thereby accelerating the kinetics at the electrode. Consequently, high-temperature operation can utilize thermal sources and it demands less electric power. Moreover, in this case, CO and O₂ could be separately produced from CO₂, and both have important industrial uses. For example, CO gas in combination with steam or other H₂ sources can be utilized as an alternative syngas for direct energy production or in the Fischer–Tropsch (F–T) process to generate various hydrocarbons.^[14]

When an oxide ion conductor is used as an electrolyte in SOECs for CO₂ electrolysis, CO₂ molecules are electrocatalytically reduced to CO at the cathode (fuel electrode). Simultaneously, oxygen ions are transported through the electrolyte to the anode (oxygen electrode), wherein gaseous pure O₂ is produced and released at a high temperature, as shown in **Figure 1a**.^[13] For CO₂ electrolysis in SOECs, the electrochemical reaction

Dr. S. Lee, M. Kim, Dr. T. H. Shin
Department of Energy and Environmental Division
Korea Institute of Ceramic Engineering and Technology (KICET)
Jinju-Si, Gyeongsangnam-do 52851, Republic of Korea
E-mail: ths@kicet.re.kr

Prof. K. T. Lee
Department of Mechanical Engineering
Korea Advanced Institute of Science and Technology (KAIST)
Daejeon 34141, Republic of Korea
E-mail: leekt@kaist.ac.kr

Prof. J. T. S. Irvine
School of Chemistry
University of St Andrews
St Andrews, Fife KY16 9ST, UK

 The ORCID identification number(s) for the author(s) of this article can be found under <https://doi.org/10.1002/aenm.202100339>.

© 2021 The Authors. Advanced Energy Materials published by Wiley-VCH GmbH. This is an open access article under the terms of the Creative Commons Attribution-NonCommercial-NoDerivs License, which permits use and distribution in any medium, provided the original work is properly cited, the use is non-commercial and no modifications or adaptations are made.

DOI: 10.1002/aenm.202100339

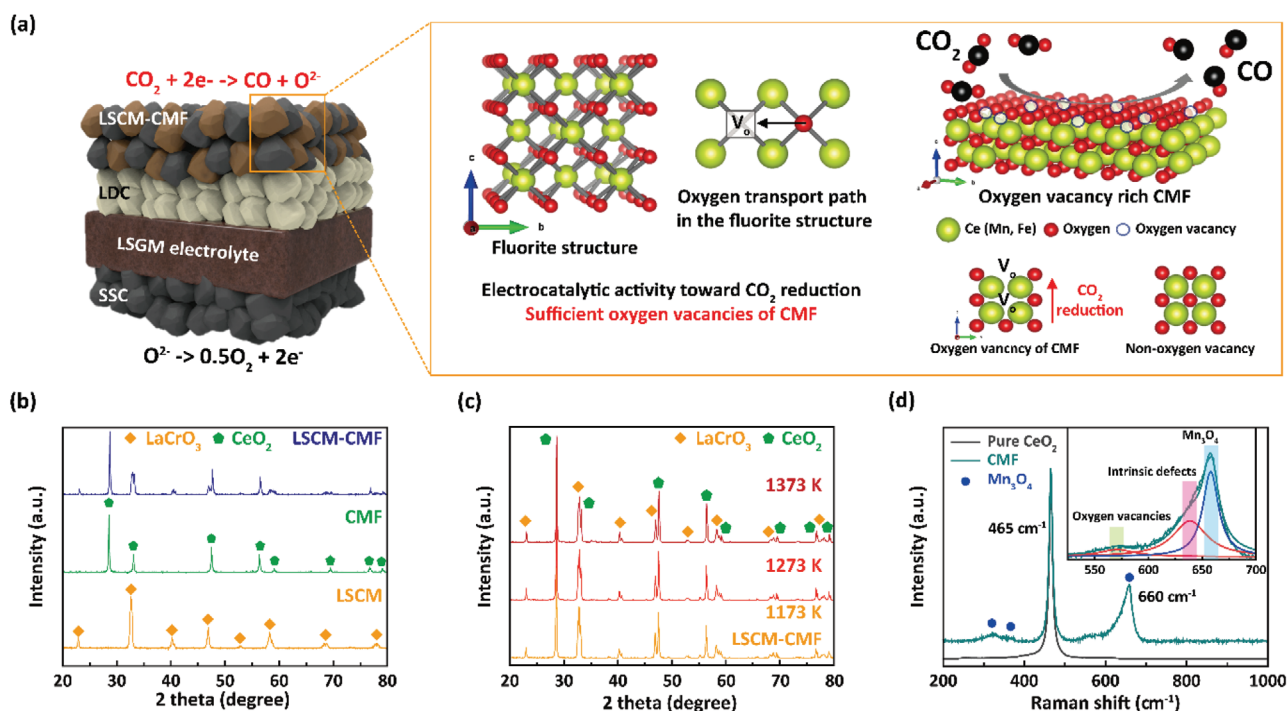


Figure 1. a) Schematic of CO₂ electrolysis on an LSGM electrolyte-based SOEC cell with an LSCM-CMF composite oxide electrode. During CO₂ electrolysis over the LSCM-CMF electrode, CO₂ molecules are adsorbed on the surface via the lattice oxygen adjacent to the oxygen vacancies, thereby forming carbonate intermediates in the ceria-based fluorite structure. Generally, doped or nanosized ceria promote the formation of oxygen vacancy defects. b) XRD patterns of different fabricated electrode materials: LSCM, CMF, and LSCM-CMF composite. c) XRD patterns measured from 1173 to 1373 K, showing the chemical compatibility between the LSCM and CMF. d) Raman spectra of the CeO₂ sample and synthesized CMF powders, which were synthesized via solid-state reaction.

is mostly dominated by the cathode reaction related to the CO/CO₂ redox couple on the electrode surface. SOECs mostly utilize materials and techniques relevant to solid oxide fuel cells (SOFCs), as they operate in the reverse mode of SOFCs. However, some materials have not been specifically tailored for CO₂ electrolysis conditions. Thus, several research groups have extensively searched for durable fuel electrodes that are suitable for both SOFC and SOEC conditions and provide high catalytic reactivity compared to the Ni-based blending electrodes for SOFCs.^[15–21] The Ni-based cathode (fuel electrode) is easily deactivated by re-oxidation or carbon formation when directly exposed to the CO/CO₂ redox reaction and hydrocarbon atmosphere.^[22,23] Therefore, the alternative cathode should have catalytic activity and electrical conductivity, and durability in terms of CO/CO₂ redox reaction. Consequently, redox stability and carbon coking tolerance have been considered as main factors when developing robust ceramic cathode (fuel electrode) candidates for CO₂ electrolysis in SOECs. Several conductive perovskite oxides have been reported to display re-oxidation resistance and coke tolerance as perovskite-type fuel electrode materials for the anode in SOFCs as well as the cathode in SOECs.^[13–20] Among them, La(Sr)Cr(Mn)O_{3-δ} (LSCM) is one of the promising cathode materials for hydrocarbon-typed SOFCs because of its high redox stability and acceptable conductivity under the reducing conditions.^[24] Irvine and Yue reported (La_{0.75}Sr_{0.25})_{0.97}Cr_{0.5}Mn_{0.5}O_{3-δ}/Gd_{0.1}Ge_{0.9}O_{1.95} (LSCM/GDC) as a composite ceramic cathode for CO₂ electrolysis. However the

cell performance was still insufficient without a precious catalyst metal (such as palladium) because of its lower electrical conductivity and catalytic activity than that of conventional Ni-based cermet.^[16,25]

In this study, we form a composite of LSCM and Ce(Mn, Fe)O₂ (CMF) and use it as an oxide cathode material for CO₂ electrolysis. Similar composite electrodes containing CMF have displayed enhanced electrochemical properties on the electrode surface with carbon-containing fuel.^[3,18,21] CMF, which itself contains partially substituted manganese and iron cations to enhance oxygen vacancies in the ceria-based fluorite lattice, has been previously reported as a promising ceramic anode material for SOFCs, with high catalytic activity related to surface oxidation.^[18] Its ceria-based fluorite structure may synergistically promote the electrocatalytic properties of LSCM perovskite phase, while CMF itself contains manganese and iron as doping elements.^[26] The CO₂ adsorption step on the cathode surface may play an important role in CO₂ electrolysis.^[27] When ceria-based CMF, including manganese and iron dopants, is introduced into the LSCM cathode material, it is expected to display enhanced CO₂ adsorption ability, surface oxidant catalytic activity, and electrocatalytic activity. The performance of LSCM-CMF composite oxide electrode was characterized, and this approach was effective for improving the electrocatalytic activities of the cathode for CO₂ electrolysis in SOECs without adding any precious metal catalyst.

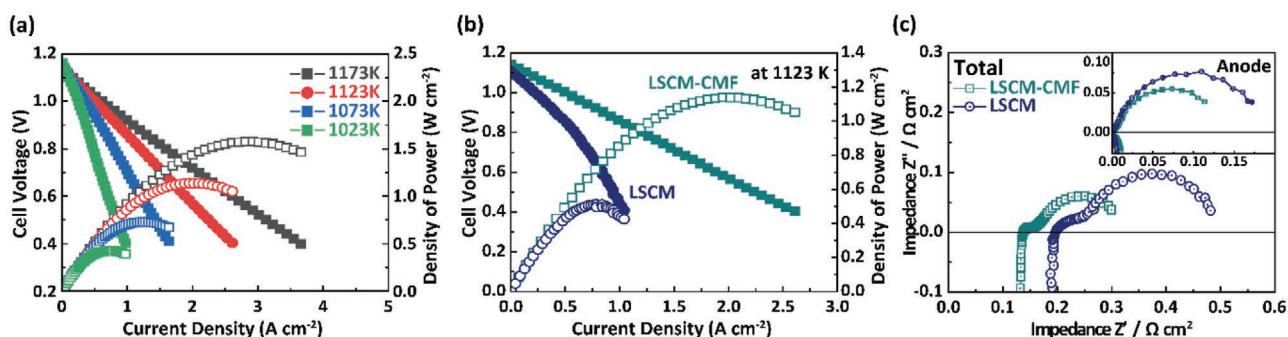


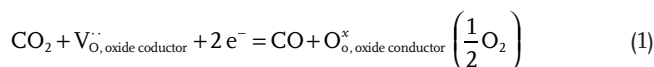
Figure 2. DC polarization (I - V) curves and EIS data in the SOFC mode. a) Performance of cell with the LSCM-CMF anode (fuel electrode) at various operating temperatures (1023–1173 K). b) Comparison of the cell performance with the LSCM-CMF and LSCM anodes at 1123 K. c) Area-specific resistances of the cell with the LSCM and LSCM-CMF anode; the inset shows a comparison with the polarizational resistance of the anode, separated by three-electrode measurement.

2. Results and Discussion

2.1. Effects of Composite Oxides with LSCM-CMF Electrode

Although the final electrode microstructure is affected by fabrication parameters such as the raw powder materials and sintering temperature, the composite material is the most important factor. We focused on the LSCM-CMF composite oxide material, because its composition and microstructure could enhance the high-temperature stability and coking resistance. Figure 1a illustrates the CO_2 reduction reaction. During CO_2 electrolysis over the LSCM-CMF electrode, CO_2 molecules are adsorbed on the surface via lattice oxygen adjacent to the oxygen vacancies to form carbonate intermediates in the ceria-based fluorite structure because the acceptor-doped ceria-based fluorite structure promotes the formation of oxygen vacancy defects.^[28,29] Generally, doping or nanosized ceria are well to enhance the presence of oxygen vacancy defects. The increased number of oxygen vacancy defects in CMF distributed with the LSCM cathode is confirmed by the Raman spectra shown in Figure 1d. The spectra have been normalized by the most intense peak, namely, the F_{2g} peak, located at $\approx 465\text{ cm}^{-1}$ and ascribed to the symmetric stretch mode of the Ce-O_8 crystal unit, which is the characteristic of the fluorite lattice structure of ceria-based materials.^[30–33] Besides the F_{2g} band, new defect-induced bands can be identified in the $525\text{--}700\text{ cm}^{-1}$ range that are not present in commercial CeO_2 powder. As shown in Figure 1d, the band at 637 cm^{-1} corresponds to manganese- and iron-doped ceria. Because the position of this band depends on the doping element, it is probably linked to the intrinsic defects generated by the dopant addition.^[31,32] Finally, the band detected at $\approx 570\text{ cm}^{-1}$ is much weaker than that detected at 637 cm^{-1} . This component is usually assigned to oxygen vacancies coupled with the presence of Ce^{3+} or other aliovalent cations.^[34–36] In addition, the bands at 320 , 375 , and 660 cm^{-1} identified in the spectra of manganese- and iron-doped ceria are presumably related to Mn_3O_4 , as shown in the Raman spectrum of Mn-doped CeO_2 in Figure S1 in the Supporting Information. Therefore, it is reasonable to infer that the sites with oxygen vacancy defects at the triple-phase boundary (TPB) might affect the chemi-absorption steps with enhancing oxygen supply. The carbonate intermediates accept electrons and subsequently dissociate into CO and O^{2-} at the surface of the LSCM-CMF as

the active site. The cathodic CO_2 reduction reaction is usually expressed as follows



Finally, CO desorbs from the surface, while O^{2-} is incorporated into oxygen vacancies and moves to the electrolyte.^[37] Based on the proposed mechanism, mixing CMF with LSCM is expected to enhance the electrocatalytic activity toward CO_2 reduction, because ceria with a fluorite structure provides several reaction sites by possessing sufficient oxygen vacancies and increasing the electronic conductivity of the cathode electrode.^[18] Figure 1b shows the X-ray diffraction (XRD) patterns of the fabricated electrode powders of LSCM, CMF, and LSCM-CMF prepared via solid-state reaction at 1473 K in air. The diffraction peaks of both perovskite and fluorite structures were observed without any impurity peaks, indicating the successful synthesis of single-phase LSCM and CMF.^[18,38] Moreover, the chemical compatibility of LSCM and CMF was investigated via XRD measurements (Figure 1c). After mixing the powders of LSCM and CMF at 50:50 wt% and firing at $1173\text{--}1373\text{ K}$ for 2 h , only diffraction peaks of the LaCrO_3 and CeO_2 structures were observed without any impurity peaks, indicating that no unwanted second phase was formed in either material. In addition, there are no any impurity peaks in the high magnification of the specific range from 24° to 34° as shown is Figure S2 in the Supporting Information.

Figure 2a shows the temperature-dependent performance of the cell with the LSCM-CMF composite oxide electrode operated at $1023\text{--}1173\text{ K}$ using 3% humidified hydrogen as fuel (SOFC mode). The open-circuit voltages (OCVs) were 1.162 , 1.150 , 1.143 , and 1.140 V , at 1023 , 1073 , 1123 , and 1173 K , respectively, and these values are close to the theoretical values predicted by the Nernst equation when wet H_2 and pure O_2 are used as each reductant and oxidant.^[39] Notably, compared to the cell performance of LSCM fuel electrode shown in Figure 2b, the cell performance after mixing CMF with LSCM (maximum powder density at the fuel cell mode using humidified hydrogen: from 0.515 to 1.139 W cm^{-2}) is drastically improved, although no precious metal catalyst was used. Figure 2c,d shows the total and anodic impedance spectra measured using

Table 1. Maximum power density and ASR for button cells with LSCM and LSCM-CMF composite oxide electrodes at 1123 K (SOFC mode) (R_s : ohmic resistance; R_p : polarizational resistance; R_{pfuel} : polarizational resistance of fuel electrode, displayed in inset of Figure 2c).

Fuel electrodes	OCV [V]	M.P.D. [W cm^{-2}]	R_s [$\Omega \text{ cm}^2$]	R_p [$\Omega \text{ cm}^2$]	R_{pfuel} [$\Omega \text{ cm}^2$]
LSCM	1.108	0.515	0.196	0.306	0.184
LSCM-CMF	1.143	1.139	0.137	0.182	0.134

the three-electrode system described in our previous report.^[18] The impedance spectrum presented more than two semicircles, which are attributed to activation, several steps of chemical reaction on the surface, and diffusion resistance. Furthermore, the ohmic resistance (R_s) is the spectral intercept with the real axis at high frequency and indicates the electrolyte resistance, whereas the total polarization resistance (R_p) is calculated from the distance between the two intercepts of the depressed arcs with the real axis. As summarized in **Table 1**, the R_p values in the total and anode impedance spectra of the LSCM-CMF composite oxide electrode are 0.182 and 0.134 $\Omega \text{ cm}^2$, much lower than those of the LSCM electrode. This result is probably owing to the enhanced surface reaction and kinetics of the high electrocatalytic activity of CMF.

According to the scanning electron microscopy (SEM) observations in **Figure 3a**, the LSCM microstructure is not significantly affected by CMF addition and the thickness of the lanthanum-doped ceria (LDC) interlayer remained at $\approx 10 \mu\text{m}$. There is no difference with perfectly same thickness between both SOEC cells as shown in Figure S3 in the Supporting Information. However, there is obviously significant difference between R_s values of LSCM and LSCM-CMF composite oxide electrode as shown in Figure 2c. This result might

explain n-type conduction behavior of CMF, which is already reported by previous works.^[40] In **Figure 3b**, all the as-prepared LSCM-CMF oxide particles presented a spherical morphology with a smooth surface. Further, uniformly distributed CMF can be identified with energy-dispersive X-ray spectroscopy (EDS) mapping and point analysis (**Figure 3c**), forming a well-connected and porous network to enhance the gas adsorption/desorption, interfacial reaction, and gas diffusion. With the dispersed CMF interacting with LSCM, this structure should be ideal for realizing a high electrocatalytic activity of CMF.

The I - V curves for the LSCM-CMF composite oxide electrode were recorded in mixed CO_2/CO gas at various compositions and at different temperatures to evaluate the electrochemical performance for electrolytic CO_2 reduction. **Figure 4** shows the I - V curves between 1023 and 1123 K using a 50:50 CO_2/CO gas with a flow rate of 100 mL min^{-1} . The figure shows a fairly linear relation between the potential and current density. We could achieve an excellent electrolysis performance using the LSCM-CMF composite oxide electrode as the current density of 2.563 A cm^{-2} at 1.5 V and 1123 K without any metal catalyst in the electrode. Compared to LSCM, the LSCM-CMF composite oxide electrode exhibits a significant increase in the CO_2 electrolysis performance in **Figure 4b**, which can be explained by the significantly

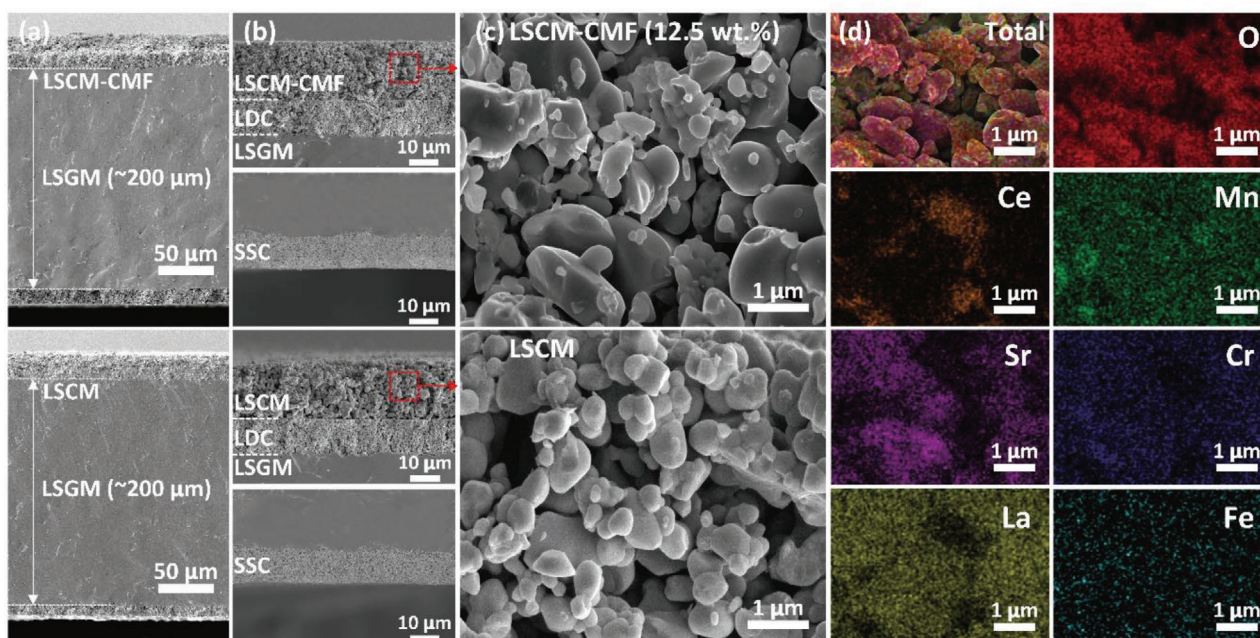


Figure 3. a) Cross-sectional images of solid oxide electrolysis cells with LSCM and LSCM-CMF. b) SEM images of the microstructure of the cell's anodic side with the LSCM and LSCM-CMF fuel electrode revealing similar thickness and morphology of each fuel electrode and LDC interlayer. c) According to the HR-SEM image of the LSCM-CMF and LSCM fuel electrode, relatively small particles are distributed on the smooth surface of spherical oxide particles resulting in d) EDS mapping identify Ce-rich oxide (CMF).

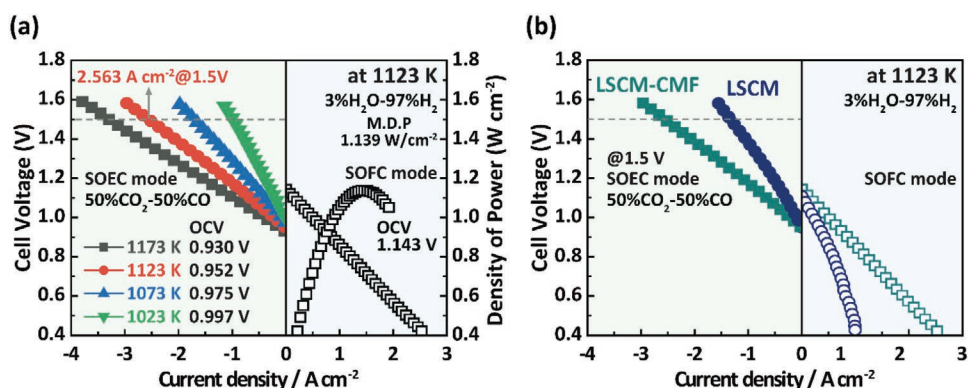


Figure 4. a) CO₂ electrolysis (SOEC) performance with the LSCM-CMF oxide electrode at various operating temperatures (1023–1123 K) using a mixed gas of CO₂/CO = 50/50 as fuel. b) Comparison of the cell performance with the LSCM and LSCM-CMF composite oxide electrodes in the SOFC and SOEC modes.

enhanced CO₂ adsorption and the subsequent dissociation processes on the designed LSCM-CMF composite oxide electrode.

For the detailed reaction mechanisms, the impedance responses of the LSCM-CMF composite oxide electrode operating in CO₂/CO mixtures at 1123 K are compared in Figure 5a,b. The impedance data were fitted using a standard equivalent circuit (displayed in the Nyquist plot) to calculate the ohmic and polarization resistance, because the real-axis intercept at the low-frequency end was not fully covered by our measured frequency range (1 MHz to 0.1 Hz). The impedance fitting results are displayed in Figure 5a. Figure 5b shows the

impedance spectra of the LSCM-CMF composite oxide electrode at different operating voltages and 1123 K in a CO₂/CO = 50/50 atmosphere. The corresponding simulated values are summarized in Table 2. Under the OCV condition, a small semicircular arc in the high-frequency region was observed with the dominant large semicircular arc in the low-frequency region. This small semicircular arc is hardly observed at other operating voltages, indicating that the impedance at low frequency, which is related to the surface adsorption/desorption processes of CO₂, dominates the overall electrochemical reduction of CO₂ compared to charge transfer processes in the high-frequency

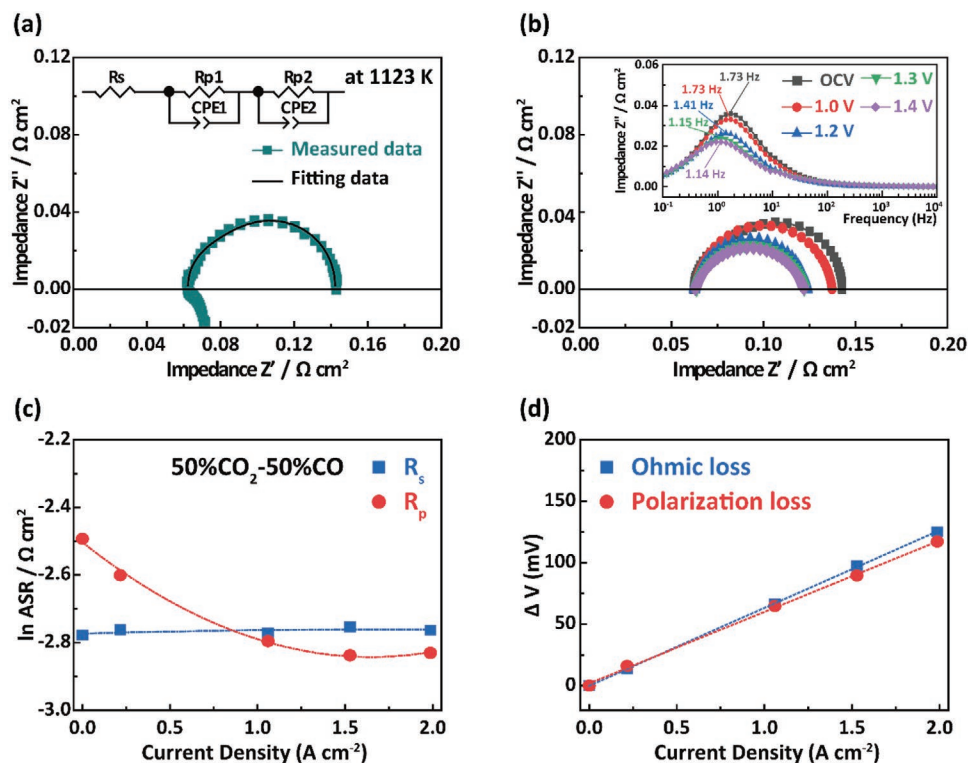


Figure 5. a) Measured and fitted impedance spectra of the LSCM-CMF composite oxide electrode with an equivalent circuit element at 1123 K. b) Nyquist plot and Bode plot from fitted impedance spectra of the LSCM-CMF composite oxide under various bias conditions. c) Ohmic and polarization resistance of the LSCM-CMF composite oxide electrode. d) Ohmic and polarization overpotential calculated from fitted EIS data.

Table 2. Fitting results of EIS data for the LSCM-CMF composite oxide electrode with applied bias under CO₂/CO = 50/50 atmosphere.

Applied bias [V]	OCV	1.0	1.2	1.3	1.4
R _s (Ω cm ²)	0.062	0.063	0.063	0.064	0.063
R _p (Ω cm ²)	0.080	0.074	0.061	0.059	0.059

region. In the study of CO₂ electrolysis using an LSCM-GDC composite oxide electrode, Irvine and Yue also observed similar types of impedance spectra;^[41] it is also known that the adsorption/desorption of CO₂ molecules on the cathode surface is the critical step in electrochemical CO₂ reduction. According to the resistance data in Figure 5c, the R_p values gradually decrease from OCV to 1.2 V and stabilize from 1.2 to 1.4 V. In contrast,

the R_s values are similar at all operating voltages. It is supposed to increasingly reduce R_p with increasing CO concentration from CO₂ reduction on the surface of LSCM-CMF. However, it seems to be the tendency of saturation at high current ranges as shown in Figure 5c. It might be supposed to be the limitation of active site number such as TPBs for CO/CO₂ electrocatalytic reaction. As shown in Figure 6b, the similar saturated

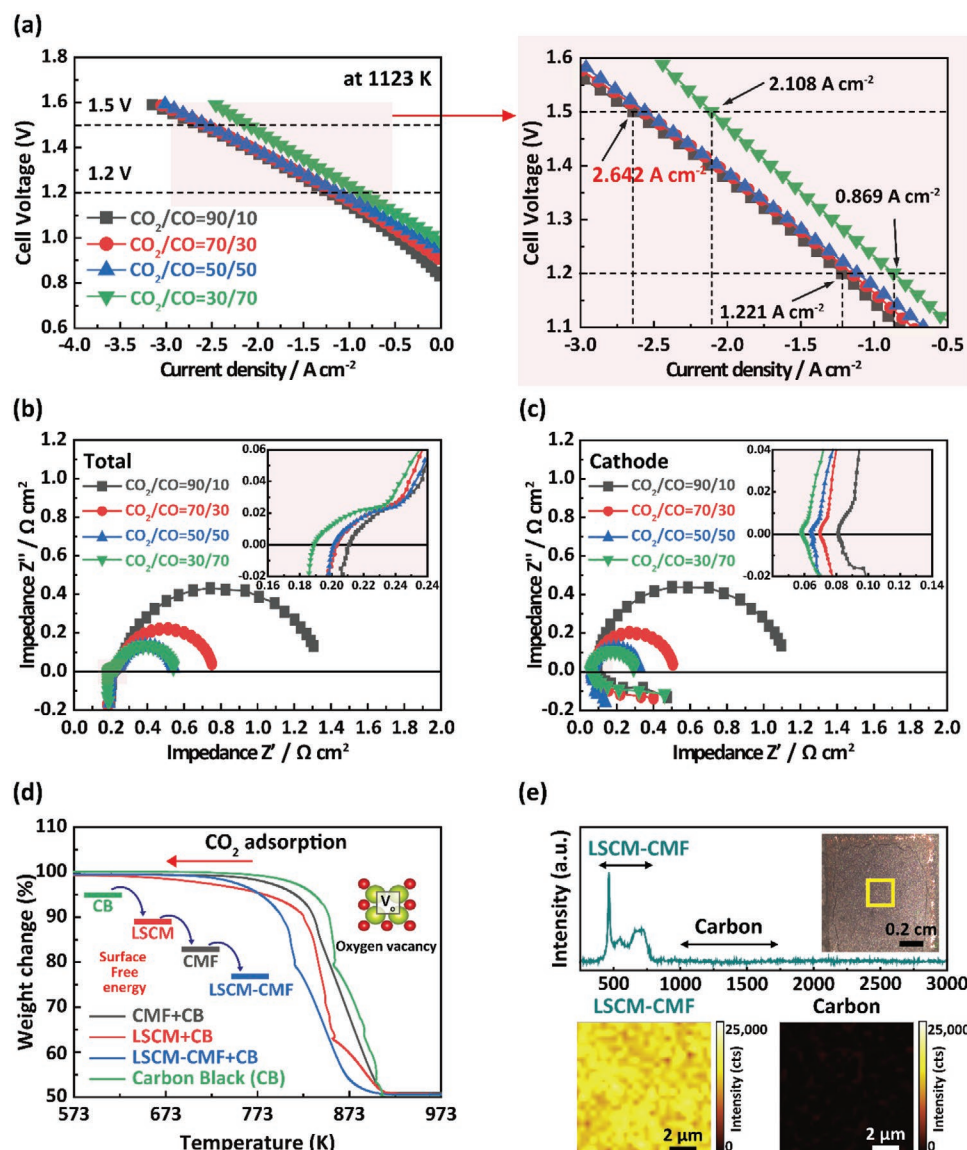


Figure 6. a) Evaluation of SOEC cell performance with the LSCM-CMF composite oxide electrode using various gas compositions at 1123 K. b) Total and c) cathodic impedance spectra of the cell with the LSCM-CMF composite oxide electrode at 1123 K. d) TGA analysis of the carbon oxidation catalytic carbon oxidation of carbon black with the CMF, LSCM, and LSCM-CMF composite oxide electrodes. e) Raman spectra collected ex situ from the LSCM-CMF oxide composite electrode after long-term analysis under CO₂ electrolysis operating conditions.

phenomenon was confirmed; the R_p value was decreased with increasing CO reaction; the reducing R_p value seems saturated from 70% of CO fraction. Figure 5d represents the ohmic and polarization voltage drop obtained from the R_s and R_p values of electrochemical impedance spectroscopy (EIS) data. It is confirmed that overpotential values from ohmic and polarizational losses, which are related to R_s and R_p , respectively, are almost the same, but ohmic loss is slightly more dominant than polarization loss at high voltage and current, as shown in Figure 5d.

Figure 6a displays the CO₂ electrolysis performance of the button cell with the LSCM-CMF composite oxide electrode at 1123 K using different CO₂/CO mixtures. The OCVs were 0.991, 0.952, 0.907, and 0.831 V for CO₂/CO compositions of 30/70, 50/50, 70/30, and 90/10, respectively. From the I - V curves of Figure 6a, the current densities for CO₂ electrolysis at 1.2 V are 1.2 and 0.869 A cm⁻² in 90/10 and 30/70 CO₂/CO atmospheres, respectively, and 2.642 and 2.108 A cm⁻² at 1.5 V, showing excellent electrolysis current densities with various CO₂/CO compositions. Unlike the I - V curves of CO₂/CO composition of 30/70, the I - V curves of the other three compositions show similar current densities above 1.2 V. According to the similar system of LSCM-GDC or LSCM-YSZ composite electrode, reported by Yue and Irvine,^[25] I - V curves with different fractions of CO₂/CO (90/10-30/70) shift in parallel with respect to the gap formed by different OCV values, implying that a high CO₂ concentration is needed for high electrolysis performance. In the case of LSCM-CMF, the initial CO₂ concentration does not significantly affect the CO₂ electrolytic performance above a certain voltage. This implies that the system can operate in a wide range of CO₂/CO ratios without significantly affecting its CO₂ electrolysis output. This fuel flexibility may originate from the outstanding catalytic activity toward CO₂ adsorption on the CMF surface. The current density of 2.642 A cm⁻² is much higher than almost all the previously reported values (0.025–1.36 A cm⁻²) for electrolyzing a CO₂/CO mixture at 1073 or 1123 K using redox-stable oxide electrode materials without any precious metal catalyst (Table S1 and Figure S4, Supporting Information). It is also higher than the value reported by Xia et al. (0.71 A cm⁻²) using an LSGM electrolyte-supported cell with LSCF-GDC composite oxide and SFM fuel electrodes.^[42] Figure 6b,c shows the total and cathodic impedance spectra at OCV and various CO₂/CO ratios. The polarization resistance tended to increase as the CO₂ concentration increased. Furthermore, the current density for CO₂ electrolysis increases with increasing cell voltage, as shown in Figure 5b, indicating a faster electrolysis reaction at a higher working potential. This behavior of decreasing polarization resistance at a higher potential is similar to the behavior of impedance reported by Yue and Irvine.^[25] This may contribute to the higher performance of CO₂ electrolysis in the range of 1.2–1.5 V when using the LSCM-CMF composite oxide electrode without any metal catalysts. The decreased polarization resistance of the oxide electrode is attributed to the enhanced catalytic activity for the surface reactions by the CMF mixing with LSCM. Thermogravimetric analysis (TGA) was conducted to confirm the enhanced catalytic activity of the LSCM-CMF composite oxide electrode, as shown in Figure 6d. Carbon black was mixed with LSCM, CMF, and LSCM-CMF (50:50 wt%) and then heated at 298–1173 K at air atmosphere. According to the TGA results,

the onset temperature of LSCM-CMF composite with oxidation of carbon black is shifted to lower temperature than those of LSCM, CMF, and pure carbon black. This suggests that the LSCM-CMF composite oxide oxidizes carbon black faster than other composites. Therefore, the improved CO₂ chemisorption properties of the LSCM-CMF composite oxide electrode accelerate the catalytic effect by reducing the surface free energy and enhancing the oxygen vacancies of CMF. Furthermore, the stable voltage behavior of the LSCM-CMF composite oxide electrode was confirmed for over 100 h under CO₂ electrolysis operating condition as shown in Figure S5 in the Supporting Information. The durability of the LSCM-CMF composite oxide electrode regarding carbon tolerance was evaluated at a constant current in CO₂ atmosphere for long-term. As shown in Figure S5b in the Supporting Information, the stable voltage behavior of the cell using LSCM-CMF under CO₂ electrolysis was confirmed for initial 20 h period and the period between 40 and 60 h, while the voltage slightly reduced after 60 h operation at 1073 K. It might be occurred by degradation of anode part or current collecting materials. Accordingly, we could confirm that no serious degradation of LSCM-CMF was observed by time dependence impedance spectra analysis of symmetric cell (LSCM-CMF|LDC|LSGM|LDC|LSCM-CMF) at the 100% CO₂ condition (Figure S5c,d, Supporting Information). Obviously, there is hardly any degradation during 100 h operation. On the other hand, the long-term test in CO₂-CO mixture condition was also conducted as shown in Figure S5e in the Supporting Information. There obviously are more stable than that of 100% CO₂ condition with no serious degradation. It might be explained by mixed oxide composite stability in middle range of partial pressure. To confirm the absence of carbon in LSCM-CMF composite oxide electrode after long-term analysis under CO₂ electrolysis operating condition, ex situ Raman analysis was conducted as shown in Figure 6e. A spectral region with LSCM-CMF between 400 and 750 cm⁻¹ was observed; however, there is no spectral region for carbon with D (1359 cm⁻¹) and G (1581 cm⁻¹). In Raman mapping, the intensity of LSCM-CMF was alone detected without the intensity of carbon. At various points for Raman mapping, the intensity of carbon was not detected as shown in Figure S6 in the Supporting Information. This indicates that there is no delamination of electrode with carbon coking under CO₂ electrolysis operating conditions. Thus, the LSCM-CMF composite oxide electrode is a stable and suitable fuel electrode for CO₂ electrolysis in SOECs.

2.2. Electrocatalytic Effects of CMF-Added LSCM for CO₂ Electrolysis

To discuss in detail for the electrocatalytic effects of CMF-added LSCM, we employed the distribution function of relaxation times (DRT) analysis since it was difficult to correctly distinguish the elementary electrode processes using EIS because of the relatively low resolution. DRT analysis was performed and subjected to complex nonlinear least square (CNLS) fitting to analyze the cell performance.^[43,44] As shown in Figure 7, three peaks, labeled P1, P2, and P4 (from high to low frequency), can be clearly distinguished in the DRT plots. Peak P3 appears at 1023 K (Figure 7c), which corresponds to electrocatalytic CO₂

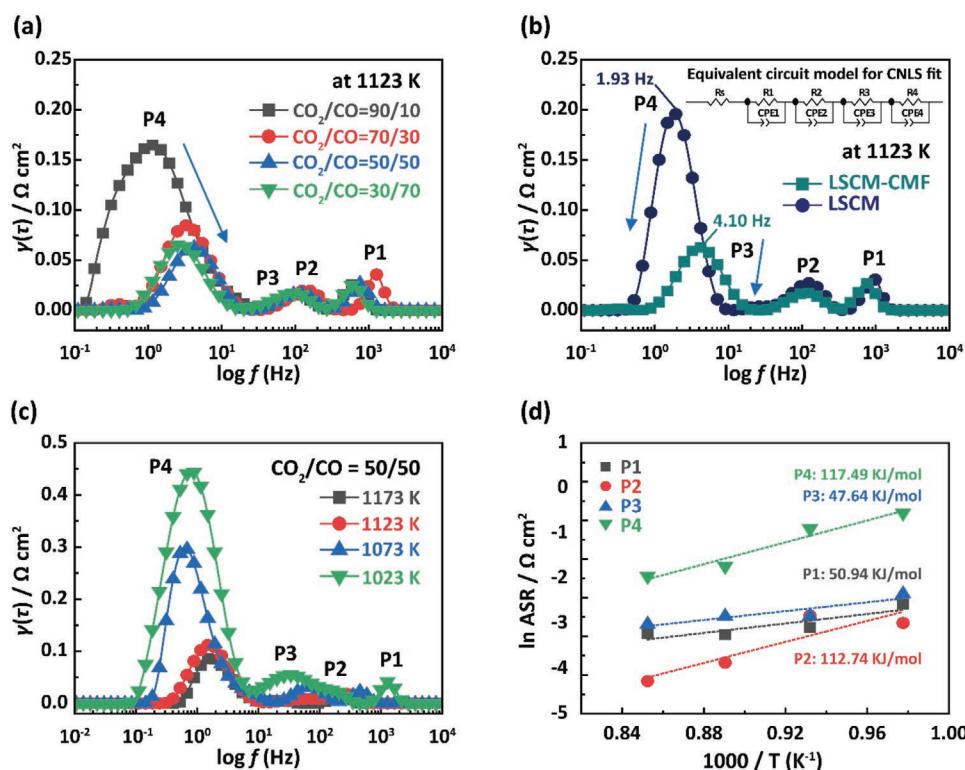
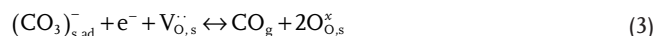
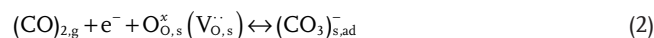


Figure 7. a) DRT plots of LSCM-CMF composite oxide electrode at different CO partial pressures, as calculated from the EIS data in Figure 6. b) Comparison of DRT plots for the LSCM-CMF composite oxide electrode and LSCM oxide electrode at 1123 K. c) DRT plots for the LSCM-CMF composite oxide electrode at different operating temperatures under mixed gas of CO₂/CO = 50/50. d) Activation energies of elementary electrode processes P1–P4 calculated from the CNLS fit results in (c).

reduction in the two cells with the LSCM-CMF and LSCM fuel electrodes. This process involves four elementary electrode processes: CO₂ adsorption on the cathode surface (P3), dissociation of the carbonate intermediate (P4), transfer of O²⁻ through the LSGM electrolyte (P1), and evolution of O²⁻ into O₂ in the anode (P2).^[45] First, the effects of CO₂/CO partial pressure on the corresponding DRT plots for the LSCM-CMF composite oxide electrode are shown in Figure 7a. Although P1 and P2 are slightly different under various CO₂/CO pressure values, the two processes are independent of the partial pressures of CO₂ and CO, whereas P3 and P4 are strongly affected by them. This suggests that P3 and P4 correspond to the cathode electrode (fuel electrode) processes. In addition, because the two cells used identical LSGM electrolytes and SSC anodes, cathode modification with the CMF oxide material mainly influenced the cathode processes P3 and P4, rather than P1 and P2. As shown in Figure 7b, the LSCM-CMF composite oxide electrode displays much accelerated P3 and P4 processes, because the area of their peaks is significantly decreased than that of the LSCM oxide electrode. This occurs because ceria with fluorite structure supplies enough adsorption sites and oxygen vacancies for the adsorption of gas molecules. Thus, for electrocatalytic CO₂ reduction occurring at the TPBs as the active sites, the CO₂ molecules are adsorbed onto the lattice oxygen adjacent to the surface oxygen vacancy and then are combined with an electron from the LSCM phase to form a carbonate intermediate (CO₃)_{s,ad}⁻ in the P3 process (Equation 2). Subsequently, in the P4 process, the carbonate intermediate accepts another electron

and forms CO, while the dissociated oxygen ion is incorporated into the oxygen vacancy to form lattice oxygen. The carbonate intermediate formed during P3 accepts an electron and then forms CO, and simultaneously, the dissociated oxygen ion is incorporated into the oxygen vacancy (Equation (3))^[46,47]



where O_{O,s}[×](V_{O,s}[•]) denotes the lattice oxygen adjacent to surface oxygen vacancy, (CO₃)_{s,ad}⁻ represents the carbonate intermediate, and O_{O,s}[×] is the lattice oxygen. Because fluorite-structured ceria possesses numerous oxygen vacancies at the surface, CMF is catalytically more active in CO₂ adsorption than the perovskite-structured LSCM, inevitably favoring processes P3 and P4. In addition, the critical role of oxygen vacancies in the formation of (CO₃)_{s,ad}⁻ suggests that the higher concentration of oxygen vacancies in the ceria-based CMF could also accelerate P3 and P4. Moreover, considering the catalytic performance and oxygen exchange property of CMF,^[48] the LSCM-CMF-gas site is more favorable than the LSCM-gas site as an active site for the dissociation of (CO₃)_{s,ad}⁻, implying that the CMF can reduce the activation energy of the P4 process. This point was confirmed by the activation energy of the P1–P4 processes for the LSCM-CMF composite oxide electrode, which

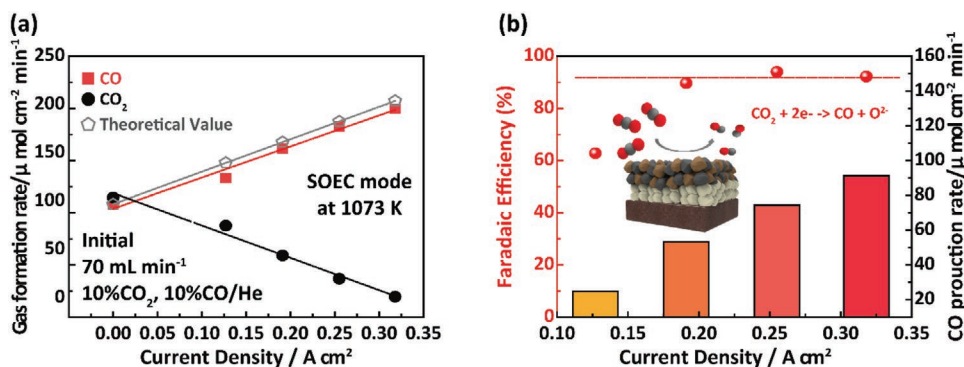


Figure 8. Gas formation rate of LSCM-CMF/LDC/LSGM/SSC SOEC cell during CO_2 electrolysis at 1073 K, measured via GC. a) Gas formation rate from CO_2 reduction as a function of the current density; and b) CO production rate and FE for electrocatalytic CO_2 reduction for different current densities.

can be obtained from the \ln ASR versus $1000/T$ plots, where ASR is the area-specific resistance. As shown in Figure 7c,d, the activation energy of P1 is $\approx 50.94 \text{ kJ mol}^{-1}$, which is lower than that of oxygen ion conduction in YZS ($106.2 \text{ kJ mol}^{-1}$) because of the high oxygen ion conductivity of LSGM.^[49] Therefore, the P1 process represents the transfer of O^{2-} in the LSGM as shown in Equation (4). Meanwhile, the activation energy of the P2 process ($112.74 \text{ kJ mol}^{-1}$) is lower than that reported for the oxygen reduction reaction on LSM-based electrodes.^[50,51] The P2 process is ascribed to the oxygen evolution reaction (Equation (5))



Based on the above results, since the two cells in this study used the same LSGM electrolyte and SSC anode, the DRT results of P3 and P4 are more reasonable than those of P1 and P3 for confirming the performance of the cathode reaction in CO_2 reduction. Characteristic frequency values between 1 and 10 Hz are presented in Figures 5b and 7b for the low frequency-assisted electrolysis voltage and existence of CMF. Especially a corresponding value of around 1.25 Hz is observed for the cathode without CMF and high voltages range, which make CO -rich condition from high current electrolysis. This low frequency might be attributed to the accelerated surface kinetics related to CO adsorption as a similar previous other report.^[16] Moreover, introduction of the CMF oxide material significantly reduced the activation energy of P4 to $117.49 \text{ kJ mol}^{-1}$ compared to other reported composite oxide electrodes (LSCM-GDC: $185.3 \text{ kJ mol}^{-1}$, CMO-based LSCM: $160.8 \text{ kJ mol}^{-1}$).^[52] Therefore, the highly active sites and abundant surface oxygen vacancies formed in CMF are responsible for the enhanced cathode electrode processes P3 and P4, resulting in reduced electrode polarization resistance for the LSCM-CMF cell.

2.3. Stability of LSCM-CMF Electrode during CO_2 Electrolysis

The outlet gas compositions were measured with different current density to evaluate the Faradaic efficiencies of the cell,

operated at 1073 K with 70 mL min^{-1} of 10% CO_2 , 10% CO in He gas. As is shown in Figure 8a, formation rate of CO gas is gradually increased with the increase in the electrolysis current and almost reaches the theoretical formation rate obtained from Faraday's law. According to Figure 8b, the Faradaic efficiency (FE) for most current densities reaches nearly 92%, suggesting that there is almost no carbon coke during CO_2 electrolysis on the LSCM-CMF cathode.

Figure 9 shows the microstructure of the cell with the LSCM-CMF composite oxide electrode after the electrochemical measurement. The SEM results indicate no substantial aggregation or delamination (Figure 9a). The mapping and point EDS results presented in Figure 9c prove that Ce-rich oxide (CMF) is well-distributed with the LSCM without much agglomeration. Ishihara et al. previously reported the stability of CMF during REDOX cycle at high temperature between Air and H_2 repeatedly through measuring the electrical conductivity and XRD during REDOX. They also reported no serious change or decomposition.^[18,40] Accordingly, there are no serious decomposition and segregation from CMF and composite electrode (LSCM-CMF) after long-term electrolysis at CO_2/CO gas (Figure S10a,b, Supporting Information) for 50 h. In order to confirm the phase stability of CMF, the XRD patterns as a function of reduction gas phase were investigated as shown in Figure S10c in the Supporting Information. However, there is also no serious decomposition peak in 5% H_2 and CO_2/CO at 1073 K even though some evitable Mn related peak is slightly detected. This implies that the developed LSCM-CMF composite oxide electrode has superior stability in CO_2 electrolysis, suggesting that CMF is stable and suitable under these conditions. Thus, the composite oxide of LSCM-CMF has a good potential for robust and coke-free cathode material with high activity toward CO_2 electrochemical reduction, replacing Ni cermet for CO_2 electrolysis in SOECs.

3. Conclusion

The dual composite oxide cathode including $\text{Ce}(\text{Mn}, \text{Fe})\text{O}_2$ (CMF) was applied in this work to enhance the catalytic activity and therefore to dramatically improve the performance of the LSCM cathode by blending CMF: LSCM-CMF as a promising robust cathode materials without any carbon coking in SOEC

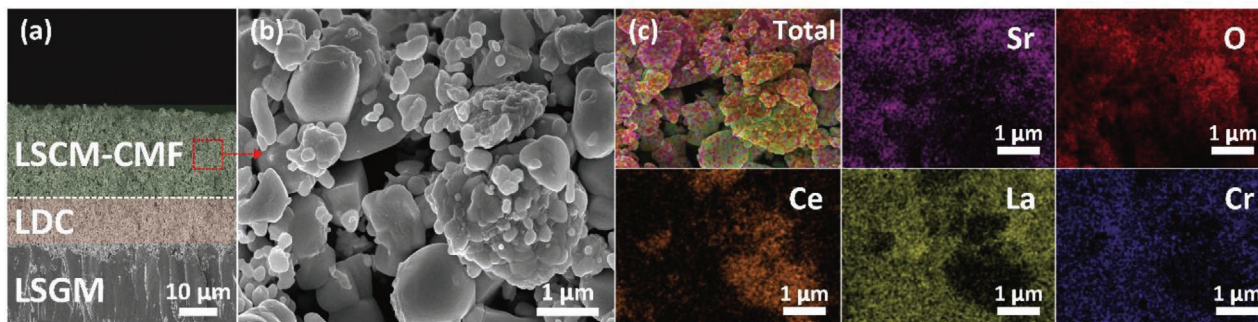


Figure 9. a) Observed microstructure and b) magnified microstructure of the button cell with the LSCM-CMF composite oxide electrode after cell operation and c) elemental distribution for the marked area in (a).

used for high-temperature CO_2 electrolysis. Its electrochemical performance was found to vary depending on the operating voltage and CO_2/CO ratio employed. When using a $\text{CO}_2/\text{CO} = 90/10$ atmosphere and an applied voltage of 1.5 V, a current density of 2.642 A cm^{-2} was obtained at 1123 K for the unit cell based on the LSCM-CMF cathode without any metal catalysts. Meanwhile, the R_p value was reduced from 0.306 to $0.184 \Omega \text{ cm}^2$. The catalytic effect of CMF greatly increased the number of active sites and surface oxygen vacancies, thereby enhancing the chemical adsorption of CO_2 on the LSCM-CMF composite oxide electrode. The DRT results demonstrated that, compared with the LSCM oxide electrode, this electrode has a much lower polarization resistance for the cathode processes. The accelerated cathode reaction by the CMF oxide material is attributed to the enhanced active sites and surface oxygen vacancy concentration for CO_2 adsorption and the subsequent $(\text{CO}_3)_{\text{s,ad}}^-$ dissociation processes. High FE of 92% is obtained with LSCM-CMF composite cathode for CO_2 electrolysis. Furthermore, the durable performance was operated with 100% CO_2 atmosphere. The results of SEM observations and ex situ Raman spectroscopy confirm that there is no carbon coking after the cell operation, indicating that the introduction of CMF in LSCM results in a promising oxide cathode material for high-temperature CO_2 electrolysis application.

4. Experimental Section

Electrode Preparation: The perovskite oxide of $(\text{La}_{0.75}\text{Sr}_{0.25})_{0.97}\text{Cr}_{0.5}\text{Mn}_{0.5}\text{O}_3$ (LSCM) and fluorite oxide of $\text{Ce}_{0.6}\text{Mn}_{0.3}\text{Fe}_{0.1}\text{O}_2$ (CMF) were synthesized by the conventional solid-state reaction from $\text{La}(\text{NO}_3)_3 \cdot 6\text{H}_2\text{O}$ (99.9%, Wako Pure Chemical Co. Ltd., Japan), $\text{Sr}(\text{NO}_3)_2$ (99%, Sigma-Aldrich, USA), $\text{Cr}(\text{NO}_3)_3 \cdot 9\text{H}_2\text{O}$ (99%, Sigma-Aldrich, USA), $\text{Mn}(\text{NO}_3)_2 \cdot 4\text{H}_2\text{O}$ (98%, Wako Pure Chemical Co. Ltd., Japan), $\text{Ce}(\text{NO}_3)_3 \cdot 6\text{H}_2\text{O}$ (98%, Wako Pure Chemical Co. Ltd., Japan), and $\text{Fe}(\text{NO}_3)_3 \cdot 9\text{H}_2\text{O}$ (99%, Wako Pure Chemical Co. Ltd., Japan) as each metal precursors. Stoichiometric amounts of each metal precursor were dissolved in distilled water under heating and stirring. After water evaporation, the ashes were pre-calcined at 673 K for 1 h to remove the remaining water and nitrates, following by calcination at 1473 K for 5 h as solid-state reaction in air to obtain crystallized powder of LSCM and CMF, respectively.

Characterization: XRD analysis (D/max 2200V/PC, Rigaku, Japan) was conducted to identify the phases in the two synthesized electrode materials and investigate their chemical compatibility. It was performed

within the 2θ range of 10° – 90° using $\text{Cu K}\alpha$ radiation ($\lambda = 1.5406 \text{ \AA}$). When investigating the chemical compatibility for mixture of LSCM and CMF at high temperature, powders of LSCM and CMF were mixed in a 50:50 weight ratio using an alumina mortar and then pressed to form a pellet, followed by heat treatment at 1173–1473 K for 2 h. SEM images were obtained with FE-SEM (JSM-7610F, JEOL, Japan) to observe the microstructure of the fabricated button cells before and after the cell operation. Raman spectroscopy (LabRAM ARAMIS, HORIBA, Japan) was conducted to investigate the difference of oxygen vacancies of commercial CeO_2 and CMF powders and to identify the carbon deposition on the surface of the LSCM-CMF composite fuel electrode after CO_2 electrolysis. The CO_2 absorption properties of LSCM, CMF, and LSCM-CMF composite oxide were investigated by TGA (Q600, TA Instruments, USA). 50:50 wt% of each powder and carbon black was mixed well and heat-treated over temperature range from 298 to 1173 K at a heating rate of $5^\circ \text{C min}^{-1}$ with Air.

Cell Preparation for CO_2 Electrolysis of SOEC: Cell tests were conducted using an electrolyte-supported button cell with a three-electrode geometry. A disk of the electrolyte was prepared by uniaxial pressing of $\text{La}_{0.8}\text{Sr}_{0.2}\text{Ga}_{0.8}\text{Mg}_{0.2}\text{O}_3$ powder (LSGM; Fuelcellmaterials, USA) at 30 MPa and sintering at 1773 K for 5 h. The sintered disk was polished to a thickness of 200 μm . The LSCM or LSCM-CMF (87.5:12.5 wt%), which was chosen as a previously optimized similar composition ratio between perovskite and fluorite composite electrodes, was ground to a fine powder using a planetary mill.^[18] $\text{Ce}_{0.6}\text{La}_{0.4}\text{O}_2$ (lanthanum-doped ceria (LDC); Dowa Electronics Materials Co. Ltd., Japan) was introduced between the fuel electrode and electrolyte as a buffer layer to block the formation of unwanted secondary phases. $\text{Sm}_{0.5}\text{Sr}_{0.5}\text{CoO}_3$ (SSC; Kceracell, South Korea) was used as the air electrode. The powdered electrode material was blended with a terpineol-based ink vehicle (Fuelcellmaterials, USA) in a ratio of 2:1 in a three-roll mill to prepare the ink, and the resulting ink was screen-printed on the LSGM electrolyte with an active area of 0.196 cm^2 . LDC buffer layer was heat-treated at 1473 K for 2 h, and the fuel electrode and air electrode were both heat-treated at 1273 K for 1 h. Pt wire was attached to the side of the air electrode as the reference electrode for the three-electrode measurement, as same to previous works.^[2,18] Consequently, the button type SOEC cell was fabricated; both the LSCM or LSCM-CMF composite oxide fuel electrode and SSC air electrode were supported on the LSGM electrolyte. LDC was used as the interlayer between the LSGM electrolyte and fuel electrode to prevent mutual element diffusion between the electrolyte and cathode during cell fabrication and operation.

Electrochemical Performance of LSGM Electrolyte-Based Cells: For cell testing, gold paste (Heraeus) was screen-printed in the shape of a grid on each surface of the electrode for current collection. The fabricated button cell was attached between two alumina pipes and sealed with a Pyrex glass ring. Each electrode containing Au grids was in contact with a Pt mesh and two pieces of Pt wires were connected to each Pt mesh for electrochemical evaluation with the four-probe method. The temperature near the cell was increased to 1173 K in air to melt the Pyrex glass sealant, following which 100 sccm of O_2 gas was fed to the air

electrode. When operating in the SOFC mode, 100 sccm of humidified H₂ gas was supplied to the fuel electrode through the bubbler, and for CO₂ electrolysis (the SOEC mode), a mixed gas of CO₂/CO was supplied. The gas flow was controlled by a digital mass flow controller. The current–voltage properties (*I*–*V* curve) and electrochemical impedance spectra were analyzed using the Solartron 1470E/14552. The impedance measurement was conducted in the frequency range of 0.1 Hz to 1 MHz. The measured EIS data were analyzed and fitted to the equivalent circuit elements using the ZView software. The composition of the outlet gas was analyzed through gas chromatography (Agilent 6890N) equipped with a Carboxen 1000 column and TCD detector.

The FE was calculated as follows

$$FE = \frac{Q_{CO}}{Q_{total}} = \frac{n_{CO}z_{CO}F}{It} \quad (6)$$

where Q_{CO} and Q_{total} represent the quantity of electricity consumed in CO production and the whole CO₂ electrolysis process, respectively; n_{CO} is the molar quantities of CO produced in CO₂ electrolysis; z_{CO} is the number of electrons transferred for a CO molecule production; F is the Faraday constant (96 485 C mol⁻¹); I is the total current in the CO₂ electrolysis process; and t is the time.

Supporting Information

Supporting Information is available from the Wiley Online Library or from the author.

Acknowledgements

S.L. and M.K. contributed equally to this work. This work was supported by the International R&D Program (grant no. P0004433) and the Technology Innovation Program (20004963) funded by Korea Institute for Advancement of Technology (KIAT), Korea Evaluation Institute of Industrial Technology (KEIT), and the Ministry or Trade, Industry & Energy (MOTIE) of the Republic of Korea. Support was also provided by the Korea Institute of Energy Technology Evaluation and Planning (KETEP) and the Ministry or Trade, Industry & Energy (MOTIE) of the Republic of Korea (No. 20182010600400).

Conflict of Interest

The authors declare no conflict of interest.

Data Availability Statement

Research data are not shared.

Keywords

Ce(Mn, Fe)O₂, composite oxide, fuel electrodes, La(Sr)Cr(Mn)O₃, solid oxide electrolysis cells

Received: January 29, 2021

Revised: April 20, 2021

Published online:

- [1] C. L. Quéré, R. B. Jackson, M. W. Jones, A. J. P. Smith, S. Abernethy, R. M. Andrew, A. J. De-Gol, D. R. Willis, Y. Shan, J. G. Canadell, P. Friedlingstein, F. Creutzig, G. P. Peters, *Nat. Clim. Change* **2020**, *10*, 647.

- [2] Z. Liu, P. Ciais, Z. Deng, R. Lei, S. J. Davis, S. Feng, B. Zheng, D. Cui, X. Dou, B. Zhu, R. Guo, P. Ke, T. Sun, C. Lu, P. He, Y. Wang, X. Yue, Y. Wang, Y. Lei, H. Zhou, Z. Cai, Y. Wu, R. Huo, T. Han, J. Xue, O. Boucher, E. Boucher, F. Chevallier, K. Tanaka, Y. Wei, et al., *Nat. Commun.* **2020**, *11*, 5172.
- [3] T. H. Shin, J. H. Myung, K. M. Naeem, C. Savaniu, J. T. S. Irvine, *Solid State Ionics* **2015**, *275*, 106.
- [4] S. D. Ebbesen, M. Mogensen, *J. Power Sources* **2009**, *193*, 349.
- [5] C. Graves, S. D. Ebbesen, M. Mogensen, K. S. Lackner, *Renewable Sustainable Energy Rev.* **2011**, *15*, 1.
- [6] S. H. Jensen, C. Graves, M. Mogensen, C. Wendel, R. Braun, G. Hughes, Z. Gao, S. A. Barnett, *Energy Environ. Sci.* **2015**, *8*, 2471.
- [7] G. Centi, S. Perathoner, *Catal. Today* **2009**, *148*, 191.
- [8] S. Garg, M. Li, A. Z. Weber, L. Ge, L. Li, V. Rudolph, G. Wang, T. E. Rufford, *J. Mater. Chem. A* **2020**, *8*, 1511.
- [9] D. W. DeWulf, T. Jin, A. J. Bard, *J. Electrochem. Soc.* **1989**, *136*, 1686.
- [10] K. Hara, A. Kudo, T. Sakata, *J. Electroanal. Chem.* **1995**, *391*, 141.
- [11] H. Yano, F. Shirai, M. Nakayama, K. Ogura, *J. Electroanal. Chem.* **2002**, *533*, 113.
- [12] A. O. Isenberg, *Solid State Ionics* **1981**, *3–4*, 431.
- [13] T. H. Shin, J. H. Myung, M. Verbraeken, G. Kim, J. T. S. Irvine, *Faraday Discuss.* **2015**, *182*, 227.
- [14] L. Chen, F. Chen, C. Xia, *Energy Environ. Sci.* **2014**, *7*, 4018.
- [15] L. Ye, C. Pan, M. Zhang, C. Li, F. Chen, L. Gan, K. Xie, *ACS Appl. Mater. Interfaces* **2017**, *9*, 25350.
- [16] X. Yue, J. T. S. Irvine, *J. Mater. Chem. A* **2017**, *5*, 7081.
- [17] L. Zhang, S. Hu, W. Li, Z. Cao, H. Liu, X. Zhu, W. Yang, *ACS Sustainable Chem. Eng.* **2019**, *7*, 9629.
- [18] T. H. Shin, S. Ida, T. Ishihara, *J. Am. Chem. Soc.* **2011**, *133*, 19399.
- [19] T. H. Shin, Y. Okamoto, S. Ida, T. Ishihara, *Chem. - Eur. J.* **2012**, *18*, 11695.
- [20] S. Sengodan, S. Choi, A. Jun, T. H. Shin, Y. Ju, H. Y. Jeong, J. Shin, J. T. S. Irvine, G. Kim, *Nat. Mater.* **2015**, *14*, 205.
- [21] T. H. Shin, H. Hagiwara, S. Ida, T. Ishihara, *J. Power Sources* **2015**, *289*, 138.
- [22] B. C. H. Steele, I. Kelly, H. Middleton, R. Rudkin, *Solid State Ionics* **1988**, *28–30*, 1547.
- [23] E. P. Murray, T. Tsai, S. A. Barnett, *Nature* **1999**, *400*, 649.
- [24] S. Tao, J. T. S. Irvine, *Nat. Mater.* **2003**, *2*, 320.
- [25] X. Yue, J. T. S. Irvine, *J. Electrochem. Soc.* **2012**, *159*, F442.
- [26] C. Sun, J. A. Alonso, J. Bian, *Adv. Energy Mater.* **2020**, *11*, 2000459.
- [27] W. Qi, Y. Gan, D. Yin, Z. Li, G. Wu, K. Xie, Y. Wu, *J. Mater. Chem. A* **2014**, *2*, 6904.
- [28] R. Schmitt, A. Nanning, O. Kraynis, R. Korobko, A. I. Frenkel, I. Lubomirsky, S. M. Haile, J. L. M. Rupp, *Chem. Soc. Rev.* **2020**, *49*, 554.
- [29] J. W. Fergus, *J. Power Sources* **2006**, *162*, 30.
- [30] S. Agarwal, X. Zhu, E. J. M. Hensen, L. Lefferts, B. L. Mojet, *J. Phys. Chem. C* **2014**, *118*, 4131.
- [31] M. Dosa, M. Piumetti, S. Bensaid, T. Andana, C. Novara, F. Giorgis, D. Fino, N. Russo, *Catal. Lett.* **2018**, *148*, 298.
- [32] L. Li, F. Chen, J.-Q. Lu, M.-F. Luo, *J. Phys. Chem. A* **2011**, *115*, 7972.
- [33] T. Vinodkumar, B. G. Rao, B. M. Reddy, *Catal. Today* **2015**, *253*, 57.
- [34] E. Sartoretti, C. Novara, F. Giorgis, M. Piumetti, S. Bensaid, N. Russo, D. Fino, *Sci. Rep.* **2019**, *9*, 2875.
- [35] Y.-W. Ju, S. Ida, T. Ishihara, *RSC Adv.* **2013**, *3*, 10508.
- [36] A. Filtschew, K. Hofmann, C. Hess, *J. Phys. Chem. C* **2016**, *120*, 6694.
- [37] Q. Fu, C. Mabilat, M. Zahid, A. Brisse, L. Gautier, *Energy Environ. Sci.* **2010**, *3*, 1382.
- [38] R. Xing, Y. Wang, S. Liu, C. Jin, *J. Power Sources* **2012**, *208*, 276.
- [39] G. Chiodelli, L. Malavasi, *Ionics* **2013**, *19*, 1135.
- [40] T. H. Shin, P. Vanalabhpatana, T. Ishihara, *J. Electrochem. Soc.* **2010**, *157*, B1896.

- [41] X. Yue, J. T. S. Irvine, *ECS Solid State Lett.* **2012**, *15*, B31.
- [42] Y. Li, X. Chen, Y. Yang, Y. Jiang, C. Xia, *ACS Sustainable Chem. Eng.* **2017**, *5*, 11403.
- [43] H. Sumi, T. Yamaguchi, K. Hamamoto, T. Suzuki, Y. Fujishiro, *J. Power Sources* **2013**, *226*, 354.
- [44] X. Zhang, L. Liu, Z. Zhao, B. Tu, D. Ou, D. Cui, X. Wei, X. Chen, M. Cheng, *Nano Lett.* **2015**, *15*, 1703.
- [45] P. Caliandro, A. Nakajo, S. Diethelm, J. Van herle, *J. Power Sources* **2019**, *436*, 226838.
- [46] Z. A. Feng, M. L. Machala, W. C. Chueh, *Phys. Chem. Chem. Phys.* **2015**, *17*, 12273.
- [47] Y. Yu, B. Mao, A. Geller, R. Chang, K. Gaskell, Z. Liu, B. W. Eichhorn, *Phys. Chem. Chem. Phys.* **2014**, *16*, 11633.
- [48] J. Zhao, X. Xu, W. Zhou, I. Blakey, S. Liu, Z. Zhu, *ACS Appl. Mater. Interfaces* **2017**, *9*, 33758.
- [49] B. Liu, H. Muroyama, T. Matsui, K. Tomida, T. Kabata, K. Eguchi, *J. Electrochem. Soc.* **2010**, *157*, B1858.
- [50] Y. Li, B. Hu, C. Xia, W. Q. Xu, J. Lemmon, F. Chen, *J. Mater. Chem. A* **2017**, *5*, 20833.
- [51] K. Chen, N. Ai, S. P. Jiang, *Int. J. Hydrogen Energy* **2012**, *37*, 10517.
- [52] X. Zhang, Y. Song, F. Guan, Y. Zhou, H. Lv, G. Wang, X. Bao, *J. Catal.* **2018**, *359*, 8.